Supporting Information

Defect-Assisted Photoinduced Halide Segregation in Mixed-Halide Perovskite Thin Films

*Alex J. Barker[1, §, *], Aditya Sadhanala[2, §, *], Felix Deschler[2], Marina Gandini[1], Satyaprasad P. Senanayak[2], Phoebe M. Pearce[2], Edoardo Mosconi[4,5], Andrew J. Pearson[2], Yue Wu[3], Ajay Ram Srimath Kandada[1], Tomas Leitjens[1], Filippo De Angelis[4,5], Siân E. Dutton[2], Annamaria Petrozza[1, *] Richard H. Friend[2,*]*

[1]Center for Nano Science and Technology@PoliMi, Istituto Italiano di Tecnologia, via Giovanni Pascoli 70/3, 20133, Milan, Italy.

[2]Cavendish Laboratory, University of Cambridge, JJ Thomson Avenue, Cambridge, CB3 0HE, UK

[3]Chemistry Research Laboratory, Mansfield Road, Oxford, OX1 3TA

[4]Computational Laboratory for Hybrid Organic Photovoltaics (CLHYO), CNR-ISTM, via Elce di Sotto 8, I-06123 Perugia, Italy.

[5]Computation, Istituto Italiano di Tecnologia, Via Morego 30, 16163 Genova, Italy.

§ These authors have contributed equally.

[*]E-mail: alex.barker@iit.it (A.J.B.), as2233@cam.ac.uk (A.S.), annamaria.petrozza@iit.it(A.P.) and rhf10@cam.ac.uk (R.H.F.)

Experimental Section

Sample preparation: Methyl ammonium bromide, MABr, and lead acetate, [$Pb(Ac)_2$] or [($Pb(CH_3CO_2)_2.3H_2O$ are mixed in 3:1 molar ratios in N,N-Dimethylformamide (DMF) to get a 0.5M solution of $MAPbBr_3$ precursor mixture. Methyl ammonium iodide, MAI, and lead acetate, $Pb(Ac)_2$,are mixed in 3:1 molar ratios in DMF to get a 0.5M solution of $MAPbI_3$ precursor mixture. $MAPb(I_{1-x}Br_x)_3$ [$0 \leq x \leq 1$] perovskite samples were fabricated using stoichiometric mixtures of the $MAPbI_3$ and $MAPbBr_3$ precursor solutions with the desired halide ratios and then spin-coating quartz substrates and annealing the films for 5 minutes at 100°C under nitrogen filled glove box.

The excess-halide films presented in Figure 5(b) were prepared as above, but using 5:1 molar ratios for the initial halide-bearing precursors.

The $MAPb(I_{0.15}Br_{0.85})_3$ films used for TA spectroscopy (Figure 4) we prepared using a two-step deposition technique, but exhibited the same photoinduced sub-bandgap PL behaviour as the films prepared *via* lead acetate precursor, indicating the phenomenon is not limited to samples made by a single preparation route. A PbI_2 solution in DMF (460 mg/ml) was spin-coated on glass at 2000 rpm for 60 sec. In order to obtain the crystalline PbI_2 thin film, all samples were annealed at 70°C for 30 minutes. The substrates were then dipped at room temperature for 5 minutes in a solution where both CH_3NH_3Br and $CHNH_3I$ salts were dissolved in isopropanol with a 6:1 molar ratio, starting from the two separated solutions of 10 mg/ml concentration each. The samples were finally rinsed in anhydrous isopropanol to remove the non-reacted organic precursors, and annealed for 5 minutes at 100°C. To protect the mixed halide perovskite from moisture exposure, a 600 nm thick layer of poly-methyl metacrilate in chlorobenzene was deposited on all the samples.

Photothermal deflection spectroscopy (PDS): A monochromatic pump light beam is absorbed in the sample (film on Quartz substrate), which produces a thermal gradient near the sample surface via heating induced by non-radiative relaxation. This results in a refractive index gradient in the area surrounding the sample surface, which is further enhanced by immersing the sample in an inert liquid, FC-72 Fluorinert® (3M Company). A fixed constant wavelength laser probe beam is passed through this refractive index gradient producing a deflection proportional to the amount of absorbed light at that particular wavelength, which is detected by a photo-diode and lock-in amplifier combination. Complete absorption spectra are obtained by scanning through different wavelengths of the excitation white light lamp with a monochromator.

White light bias LED: The spectrum of the white light LED used for light soaking is given at 0.2 sun (~ 20 mW cm^{-2}) in Figure S1.

PL measurements (low duty-cycle system): Time-resolved photoluminescence measurements were taken with a gated intensified CCD (iCCD) camera system (Andor iStar DH740 CCI-010) connected to a grating spectrometer (Andor SR303i). Excitation was performed with femtosecond laser pulses which were generated in a homebuilt setup by second harmonic generation (SHG) in a barium borate (BBO) crystal from the fundamental output (pulse energy 1.55 eV, pulse length 50 fs) of a Ti:Sapphire laser system (Spectra Physics Solstice). The laser pulses generated from SHG had a photon energy of 3.1 eV, pulse length ~100 fs and fluence ~1 μJ/cm^2. PL spectra were detected by accumulating several exposures on the iCCD (exposure time of 100 ms, 20 accumulations and gate width of 1 ms). Temporal resolution of the change in PL spectra on a timescale of seconds was obtained by sequential read-out of the iCCD with a frequency of 1 KHz.

PL measurements (high duty-cycle and CW measurements): Samples were excited with a PicoQuant diode laser with 40 MHz repetition rate, excitation energy 3.05 eV, fluence of ~ 46 pJ/cm^2/pulse and ~100 ps pulse length, or otherwise as described in the text. PL was collected either by spectrally dispersing the emission in a SpectraPro2500i spectrograph (Princeton Instruments) and detecting with a thermoelectrically cooled PIXIS 100-F CCD camera (Princeton Instruments), or by collecting PL into a fibre-coupled Maya2000 Pro spectrometer from Ocean Optics. Mean PL energy was found after converting the PL spectra from wavelength to energy using the Jacobian transformation.

PL measurements (excitation energy dependence):

The PL results shown in Figure 2a were collected in the same way as the high duty-cycle system described above, but excited using three CW lasers with different emission wavelengths. The intensity of each laser was varied according to the optical density of the sample in order to keep the absorbed photon flux similar in each case. The experimental parameters are shown in Table S1 below.

Table S1: Experimental parameters for excitation energy dependent PL

λ (nm)	E (eV)	Intensity (W cm^{-2})	Photon flux (cm^{-2} s^{-1})	OD	Absorbed photon flux (cm^{-2} s^{-1})	Absorbed photon flux (norm.)
635	1.95	1.89	6.02E+18	0.251	2.64E+18	1.00
532	2.33	1.53	4.09E+18	0.503	2.80E+18	1.06
450	2.76	0.68	1.54E+18	0.946	1.36E+18	0.52

X-ray diffraction measurements (XRD): XRD measurements were made on thin film samples using a Bruker D8 discover diffractometer in Bragg-Brentano mode with Cu kα radiation, $\lambda = 1.54$ Å. Full scans over a wide angular range $10 < 2\theta < 60^{o}$ with a step size of $\Delta 2\theta = 0.01^{o}$ were made on films under dark conditions (see Figure S6). Light soaking (~0.1 suns) was then added and short scans over a narrow angular range, each taking ~1 minute, were made to explore changes in the (400) and (220) reflections. Once this scan became stable under light soaking a scan over the complete angular range was measured, a similar procedure was used to explore changes in the structure once light soaking was removed.

Due to preferential alignment in the films a complete structural analysis was not possible (Figure S8). However quantitative analysis of the patterns collected over the full angular range to obtain the lattice parameters was carried out using a Le Bail analysis[1] within the FULLPROF suite of programmes.[2] Background fits were fit using a refined interpolation of points and the peak shape modelled using a pseudo-Voigt function.

GIWAXS: Experiments were performed on the I07 beamline at the Diamond Light Source, Didcot, U.K. Beam energy was 10 keV and the angle of incidence was 0.2˚. During measurement each sample was housed inside a custom built sample chamber held under a continuous overpressure of dry He. The estimated X-ray beam flux at the sample chamber was $< 10^{12}$ photons/s/0.1% b/w. Raw data was collected using a Pilatus 2M detector, with diffraction patterns collected every 14 s using an exposure time of 1 s (note that fast shutters were employed to minimize sample X-ray exposure outside of the data collection periods). Data was analysed using the DAWN software package[3] (www.dawnsci.org), with silver behenate used as a calibration standard. To minimize grid artefacts the integrated 1D

GIWAXS profiles were extracted from a ±5˚ radial profile of the 2D data, centred at 45˚ from the sample normal.

To complement these measurements additional XRD experiments were performed on the I12 beamline at the Diamond Light Source, Didcot, U.K. Here, the beamline operated in energy dispersive diffraction mode with samples held under ambient conditions during measurement. XRD patterns on the same and nominally identical samples to the initial experiment were recorded with a time resolution of 1 s whilst under constant light soaking.

Transient absorption (TA) measurements: The pump and probe pulses were both provided by a Q-switched Ti:Sapphire based regenerative amplifier (Coherent RegA 9000) operating at 250 kHz (1.55 eV, ~70 fs) seeded by a mode-locked Ti:Sapphire oscillator (Coherent Micra-18) operating at 80 MHz. For the above-gap pump pulses, the beam was focused onto a BBO crystal generating a second harmonic at 3.1 eV. Below-gap pump pulses at 1.88 eV were generated in a BBO-based collinear OPA (Coherent 9450). Broadband white light probe pulses were generated by focusing the 1.88 eV output of the amplifier into a thin sapphire plate. The pump-probe delay was adjusted *via* a variable linear delay stage. After interaction with the sample, the probe light was dispersed in a spectrometer (PI Acton SpectraPro) and collected on a Si detector array (Stresing Entwicklungsbüro). All TA was collected with samples under vacuum at room temperature. The instrument response function of the system has FWHM ~ 150 fs. The intensity of the probe pulses was always significantly lower than the pump pulses. Due to the short duty cycle of the pump and probe. Halide segregation was not induced during the TA experiments (except when intentionally induced using a CW light source), as evidenced by the lack of a sub-bandgap bleach feature in the data presented in Figure 3a.

Table S2: Changes in the lattice parameters determined from X-ray diffraction for $MAPb(I_{0.4}Br_{0.6})_3$ and $MAPb(I_{0.6}Br_{0.4})_3$ as a function of light soaking .

	$MAPb(I_{0.4}Br_{0.6})_3$			$MAPb(I_{0.6}Br_{0.4})_3$		
	Initial	With light soak	Without light soak	Initial	With light soak	Without light soak
Exposure/post exposure time (hours)	-	0.5	2.75	-	1.75	18
FWHM of peak comprised of (220) and (400) reflections (°)	0.1269	0.1626	0.1286	0.1350	0.2309	0.1455
Maximum intensity of peak comprised of (220) and (400) reflections (counts)	30528	20934	30415	14327	7955	12129
a (Å)	8.56602(8)	8.56076(11)	8.56127(10)	8.69180(2)	8.6774(2)	8.6736(2)
c (Å)	12.1236(2)	12.1199(5)	12.1145(2)	12.2856(2)	12.2532(3)	12.2596(2)
V ($Å^3$)	889.59(2)	888.23(4)	887.94(2)	928.18(3)	922.64(4)	922.30(3)
% change in V from initial state	0	-0.15	-0.11	0	-0.60	-0.63
% tetragonal distortion	0.07	0.11	0.06	0.05	0.15	0.05

The changes in the lattice parameters were determined using a Le Bail analysis[1] over the full angular range using the reported tetragonal structure[4] as a function of light soaking for $MAPb(I_{0.4}Br_{0.6})_3$ and $MAPb(I_{0.6}Br_{0.4})_3$. The results are given in Table S2 above. In both films a contraction in the unit cell volume and an increase in the % tetragonal distortion,$(\frac{(c-\sqrt{2}a)}{(c/2+a/\sqrt{2})}x100)$, with light soaking is observed. The magnitude of the changes in both the tetragonal distortion and volume, $(\frac{V_{init}-V_{new}}{V_{init}}x100)$, are observed to be significantly larger in iodide-rich $MAPb(I_{0.6}Br_{0.4})_3$ compared to bromide-rich $MAPb(I_{0.4}Br_{0.6})_3$ materials. When light soaking is removed the tetragonal distortion becomes close to that of the initial state whereas the volume contraction remains. The results are given in Table S2 above.

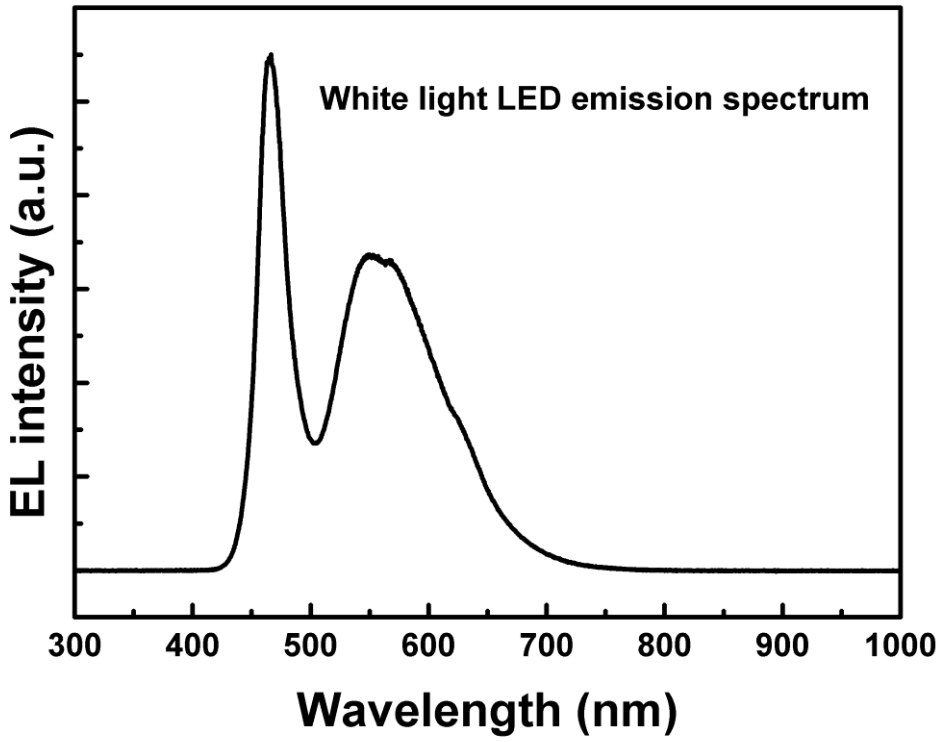


Figure S1: White light LED emission spectrum at ~0.2 sun (~20 mW/cm^2) intensities.

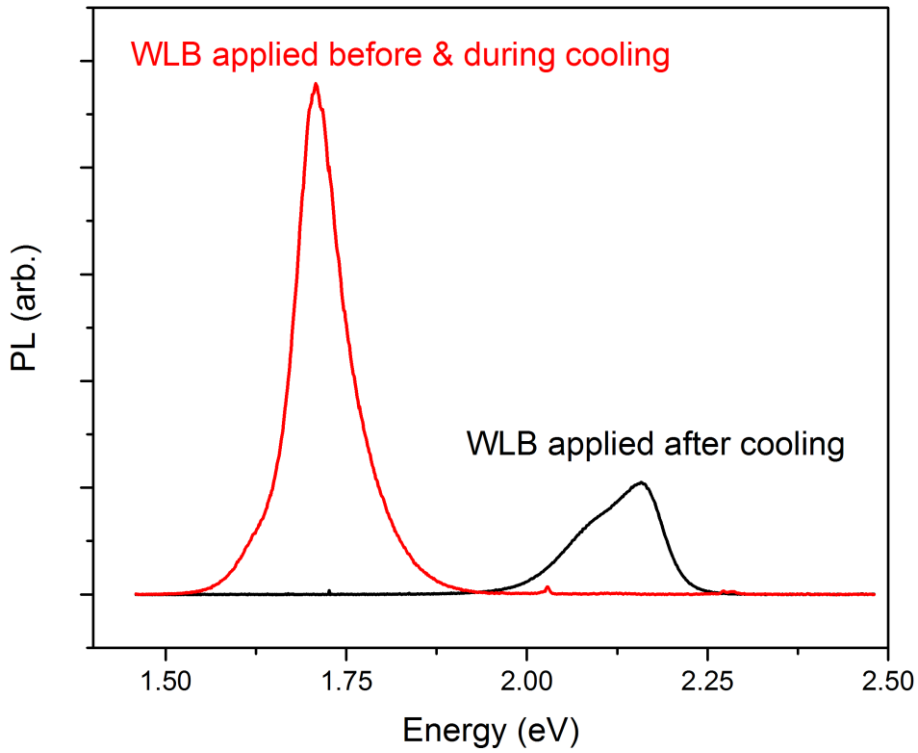


Figure S2: PL of $MAPb(I_{0.15}Br_{0.85})_3$ at 200 K with a white light bias (WLB, i.e. light soaking). If the sample is cooled before illumination, formation of the sub-bandgap PL is strongly inhibited (black line). If WLB illumination takes place prior to, and during cooling, the sub-bandgap states are formed and continue to dominate the PL at low temperature (red line).

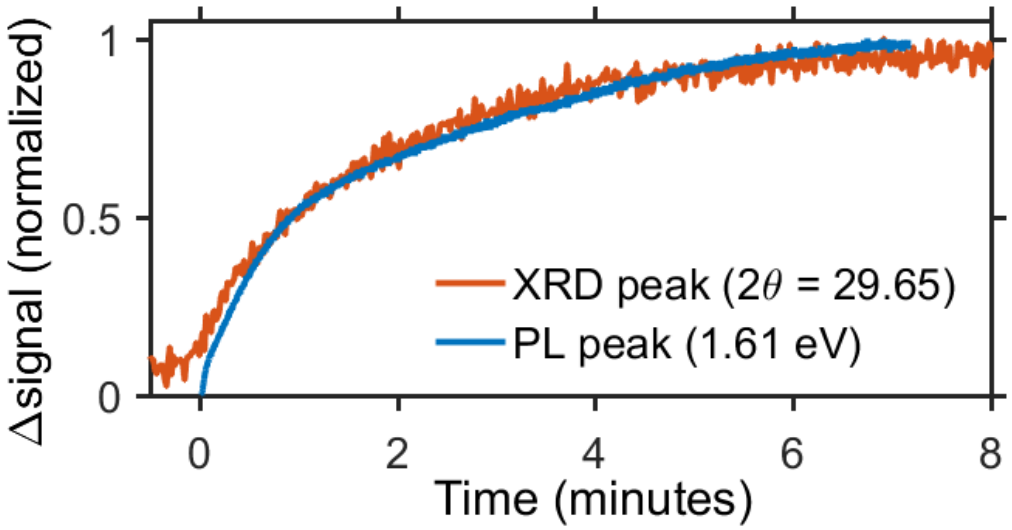


Figure S3: Evolution of the XRD peak amplitude at 2θ = 29.65˚of $MAPb(I_{0.4}Br_{0.6})_3$ upon CW illumination, overlaid with growth of the sub-bandgap PL feature.

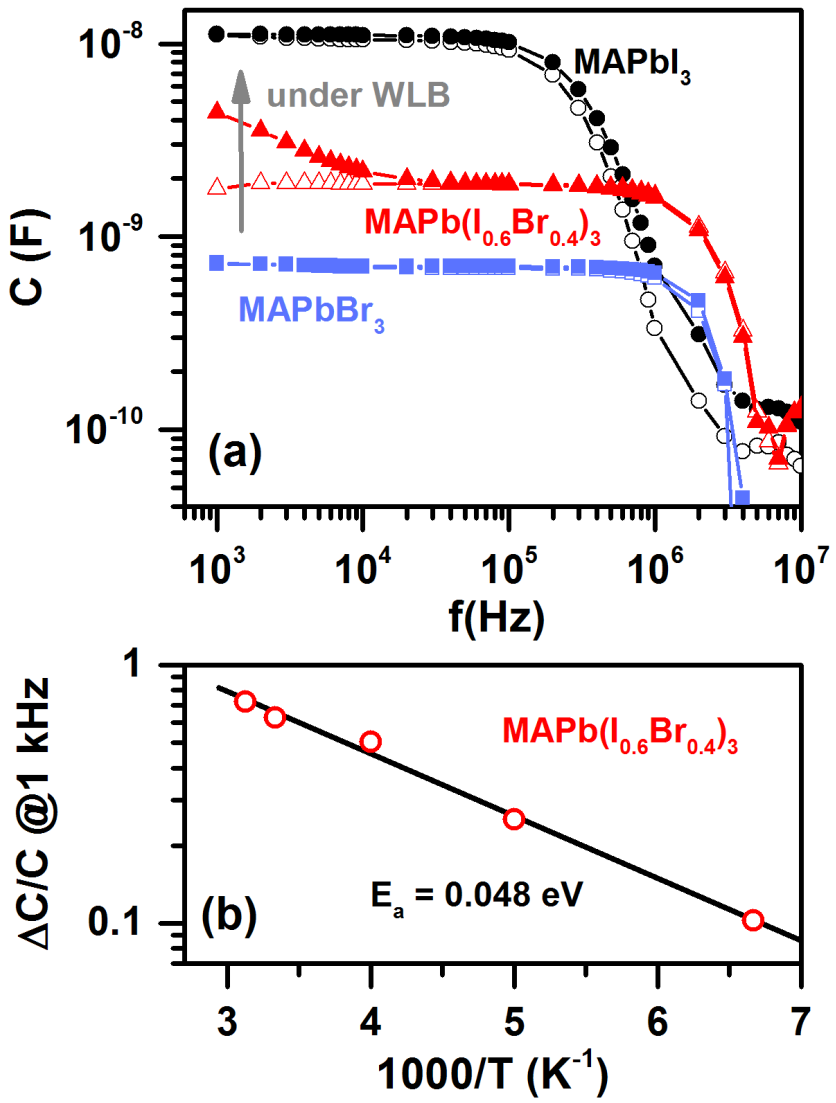


Figure S4: (a) Impedance spectroscopy of tri- and mixed-halide samples in the dark (open symbols) and under WLB light soaking (1 Sun, 30 minutes, closed symbols) respectively. (b) Temperature dependence of the photoinduced change in capacitance at 1 kHz for $MAPb(I_{0.6}Br_{0.4})_3$.

The frequency-dependent capacitance of samples with x = 0, 0.6, and 1 was measured while applying a 30 mV AC bias over a frequency range from 1 kHz to 10 MHz . Figure S4a shows that at low frequencies (1-10 KHz), the samples with the highest iodide content exhibit the highest capacitance, indicating a reduction in the degree of cooperativity and order in the molecular dipoles with increasing bromide fraction. Upon illumination, the C(ω) behaviour of the tri-iodide and tri-bromide samples remains mostly unchanged. A more drastic change is

seen in the mixed-halide (x = 0.6), where the low frequency capacitive response exhibits a strong photoinduced enhancement. This enhancement can be quantified as a differential capacitance, $\Delta C/C = (C_{light} - C_{dark})/C_{dark}$. Figure S4b shows that the low-frequency $\Delta C/C$ decreases with temperature in a fashion that is well described by an Arrhenius mechanism with a thermal activation energy of 48 meV.

Impedance Spectroscopy: Sandwich devices were fabricated with patterned Au bottom electrode on ITO substrates and shadow mask patterned top Au electrode. In order to minimize leakage and obtain reliable devices thicker perovskite films (> 0.5 μm) were utilized for the devices. Impedance measurements were performed using a standard HP 4912A Impedance Analyser over a frequency of 1 kHz to 10 MHz. The sample was illuminated with a home-made light source through the thin Au layer on the ITO side of the device.

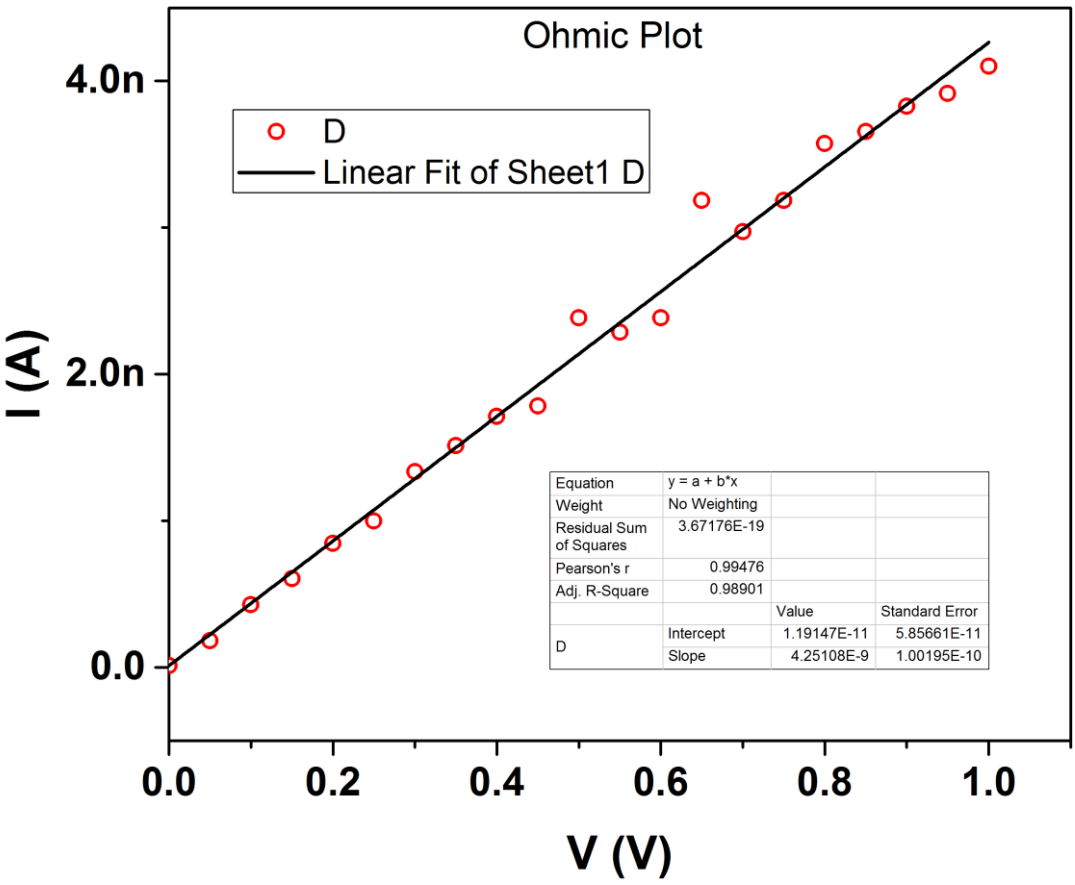


Figure S5: IV curve of the Au-MAPb($I_{0.6}Br_{0.4}$)$_3$-Au device used for the impedance spectroscopy presented in Figure S4. The device exhibits ohmic response.

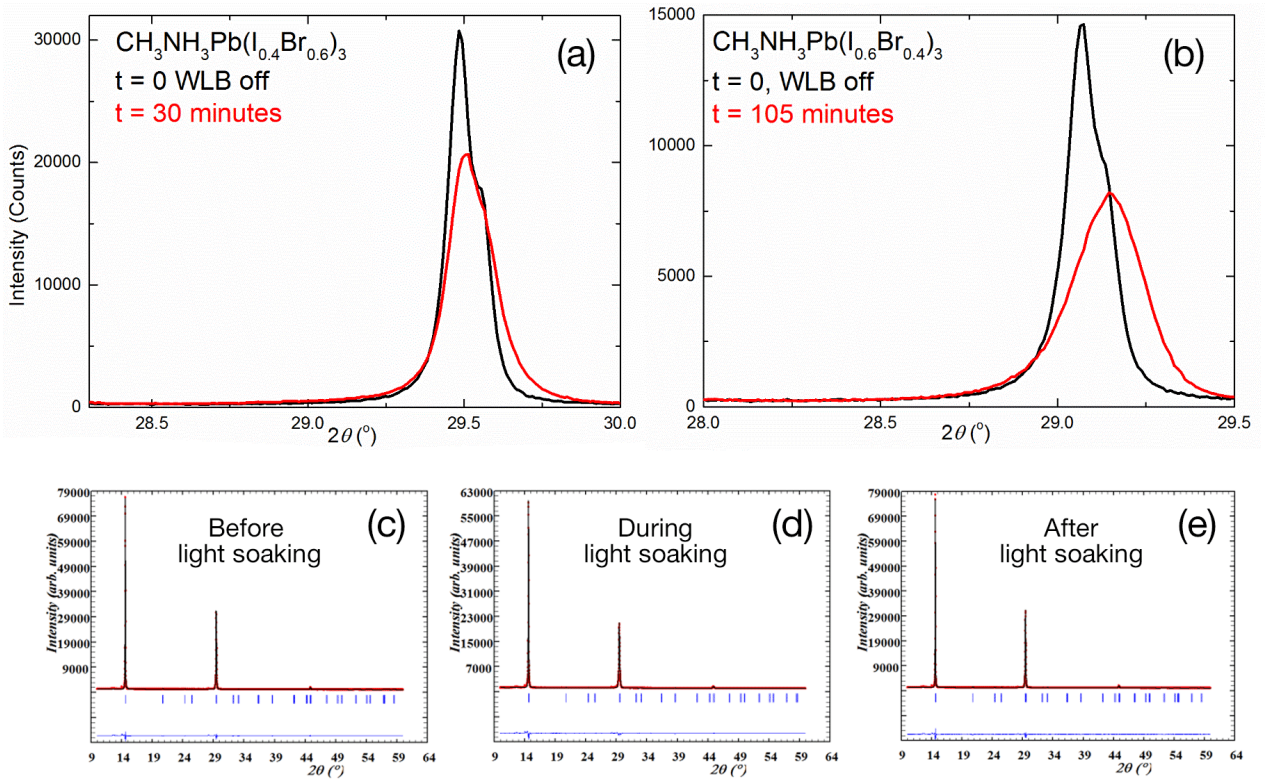


Figure S6: (a,b) XRD patterns showing the changes in the XRD of the (004) and (220) reflections for $MAPb(I_{0.4}Br_{0.6})_3$ and $MAPb(I_{0.6}Br_{0.4})_3$ before (black) and after (red) exposure to light soaking. (c,d,e) Full range XRD patterns for $MAPb(I_{0.4}Br_{0.6})_3$ perovskite thin-film - before, during light soaking (30 minute exposure), and 165 minutes after removing the light soaking.

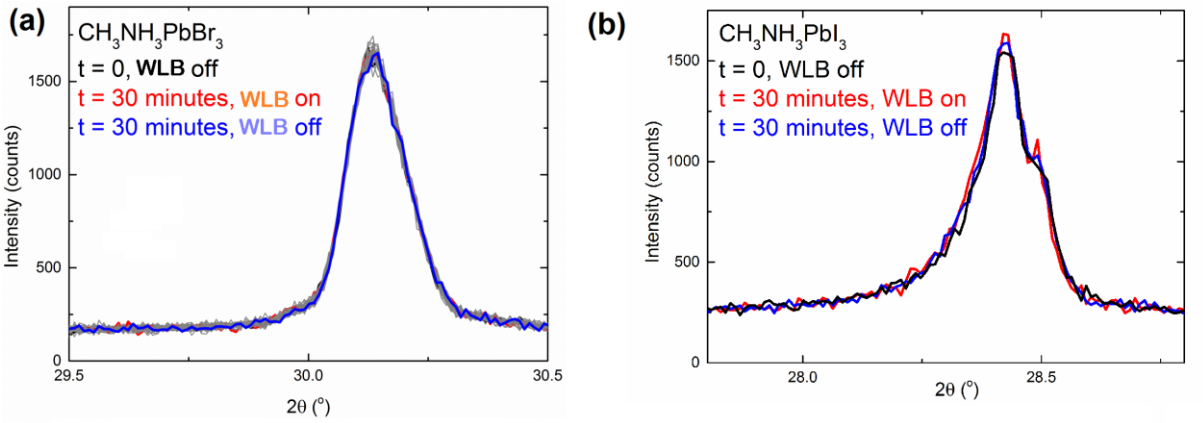


Figure S7: (a) Shows the XRD patterns and the time evolution of the (200) reflections for MAPbBr3 perovskite thin-film under WLB and after removal of WLB. (b) Shows the XRD patterns and time evolution of the and (004) and (220) reflections for MAPbI3 perovskite thin-film under WLB and after removal of WLB.

GIWAXS measurements on $MAPb(I_{1-x}Br_x)_3$ were performed to improve the resolution and selectively probe the top region of the film, where illumination (and presumably ion segregation) are more prominent. The GIWAXS results are shown in Figure S8 and point towards similar strain induced crystal structure distortion under WLB as presented in the XRD section of the main text.

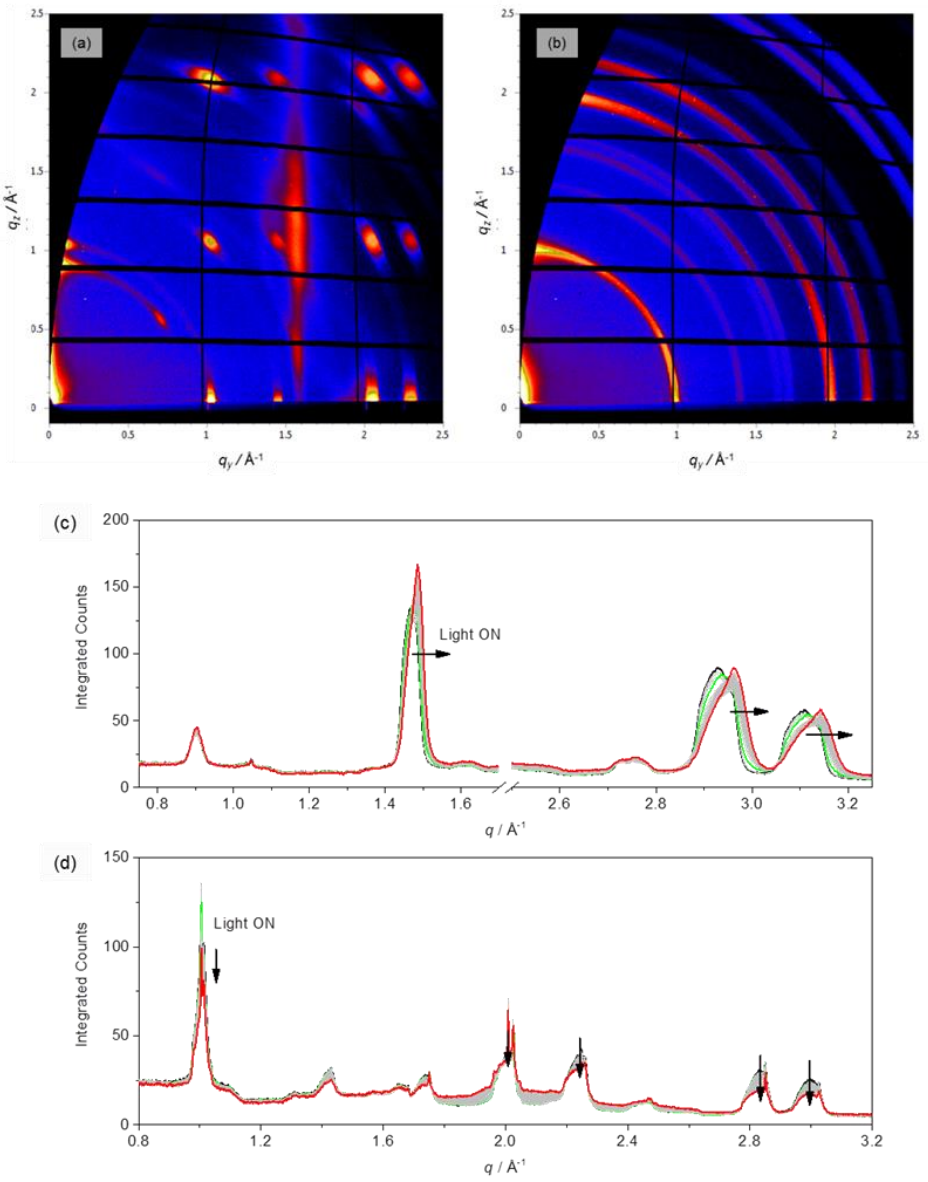


Figure S8: (a,b) 2D GIWAXS patterns for $MAPb(I_{0.4}Br_{0.6})_3$ and $MAPbI_3$ thin-films respectively. Reduced 1D scattering patterns showing the time evolution of the characteristic diffraction peaks during 10 minutes WLB for the $MAPb(I_{0.4}Br_{0.6})_3$ (part (c)) and MAPbI3 (part (d)) perovskite samples. Note that the refelction at 0.9 Å^{-1} in part (c) corresponds to residual PbI_2 in the sample. Profiles were taken from the 2D GIWAXS data using a ±5˚ radial profile centred at 45˚ from the sample normal.

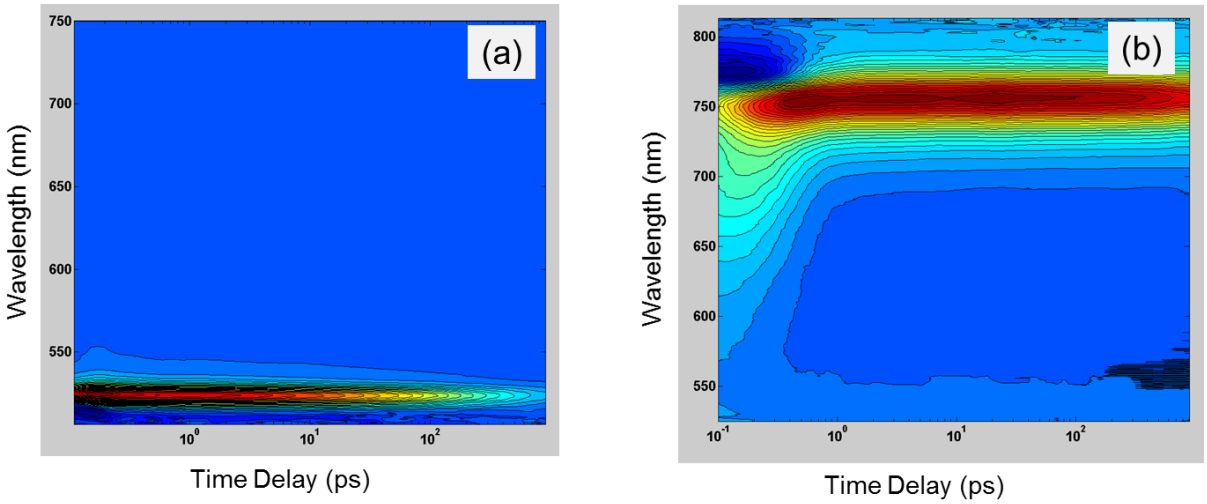


Figure S9: Ultrafast TA dynamics of $MAPbBr_3$ (a) and $MAPbI_3$ (b) perovskite films under WLB illumination of ~0.2 sun. Excitation was performed with a pulsed laser system at 2.36 eV photon energy with a fluence of ~7 μJ/cm^2/pulse.

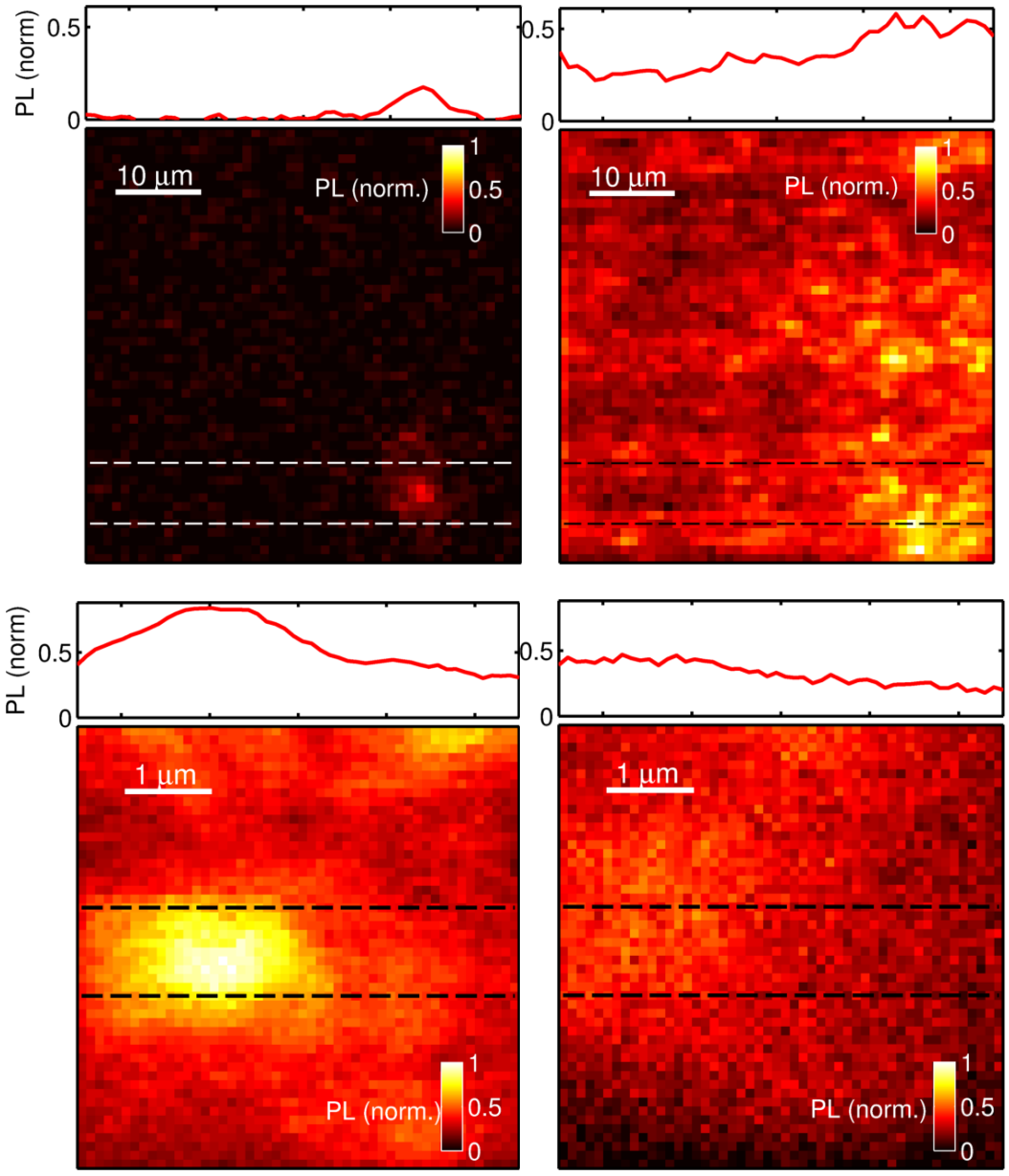


Figure S10: Confocal maps of the distribution of iodide-rich regions by collecting PL from their direct excitation at 670 nm (below the bandgap of the pristine material, with x=0.85) (a) before and (b) after light soaking with a white LED at 15 mW cm^{-2}. The bottom maps show higher magnification PL maps of a second region featuring a bright spot (c) during light soaking and (d) after 50 minutes in the dark. The top sections of each panel show the mean PL cross-section taken through the regions indicated by dotted lines on the PL maps.

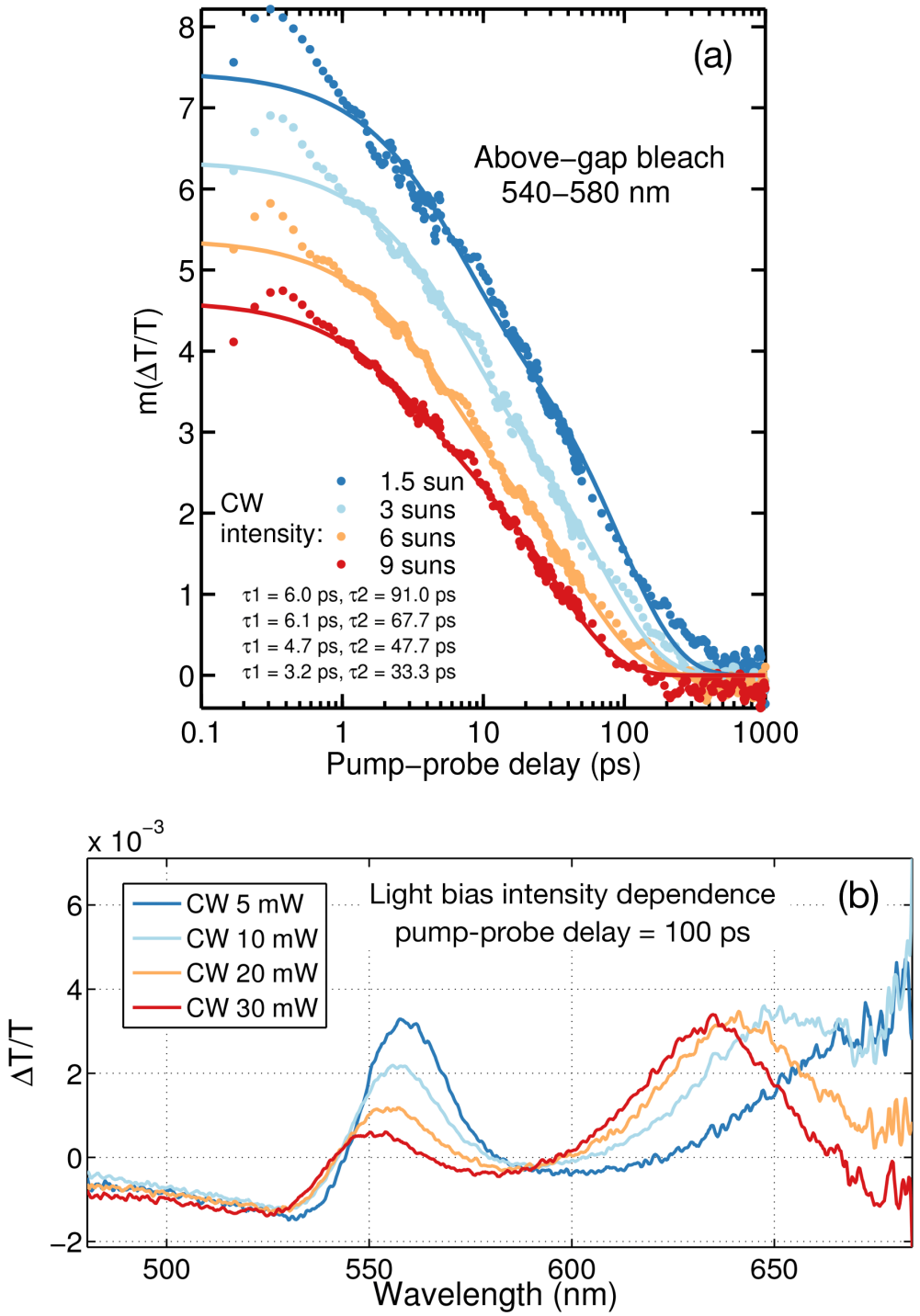


Figure S11: Ultrafast TA spectroscopy of a MAPb($I_{0.15}Br_{0.85}$)$_3$ perovskite film showing dependence of the high energy GSB (a) kinetics and (b) excited state spectral shape on light bias intensity. Note the blueshift of the low energy bleach with increasing CW light bias. As a result of increased carrier density concentration in the bromide depleted region, steady-state band filling by CW excitations prevents modulation of band edge populations by the TA pump pulse.

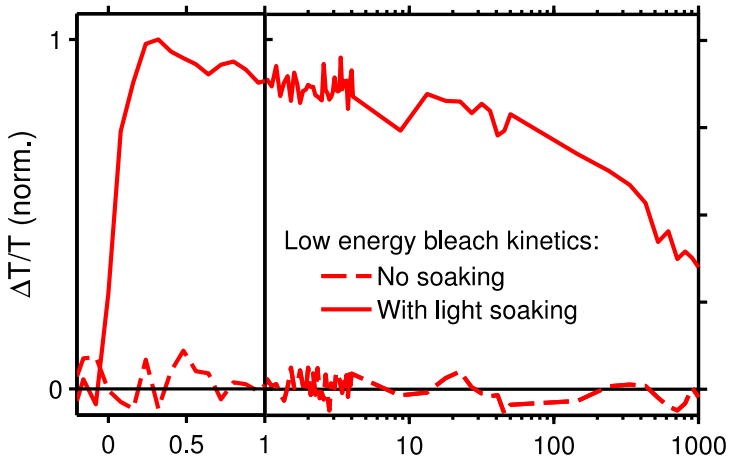


Figure S12: Ultrafast TA spectroscopy of a MAPb($I_{0.15}Br_{0.85}$)$_3$perovskite film, showing the low energy GSB kinetics under sub-gap excitation (1.88 eV), with and without light bias. In contrast to the kinetics shown in Figure 3c of the main text, under sub-gap excitation the photoinduced states are populated almost immediately (within 300 fs).

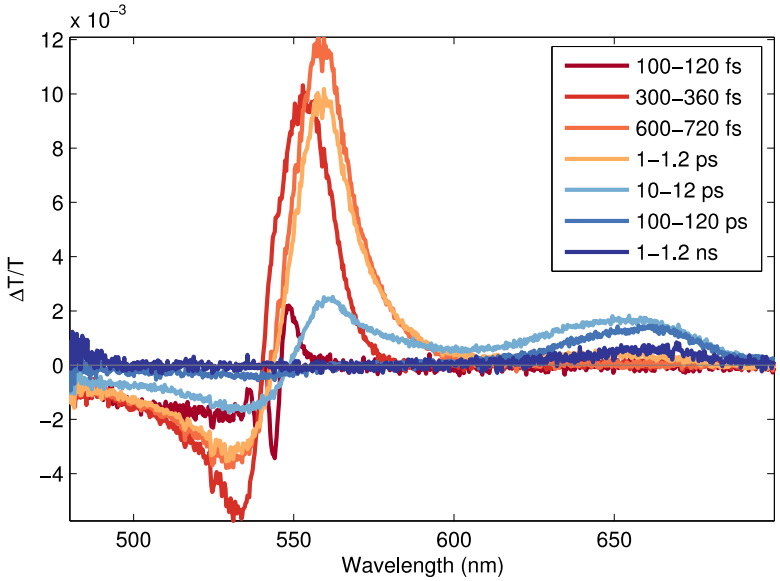


Figure S13: Ultrafast TA spectra of CsPb($I_{0.25}Br_{0.75}$)$_3$ under light bias show similar sub-bandgap phenomena, ruling out orientation effects of the methylammonium ions as necessary for sub-bandgap state formation.

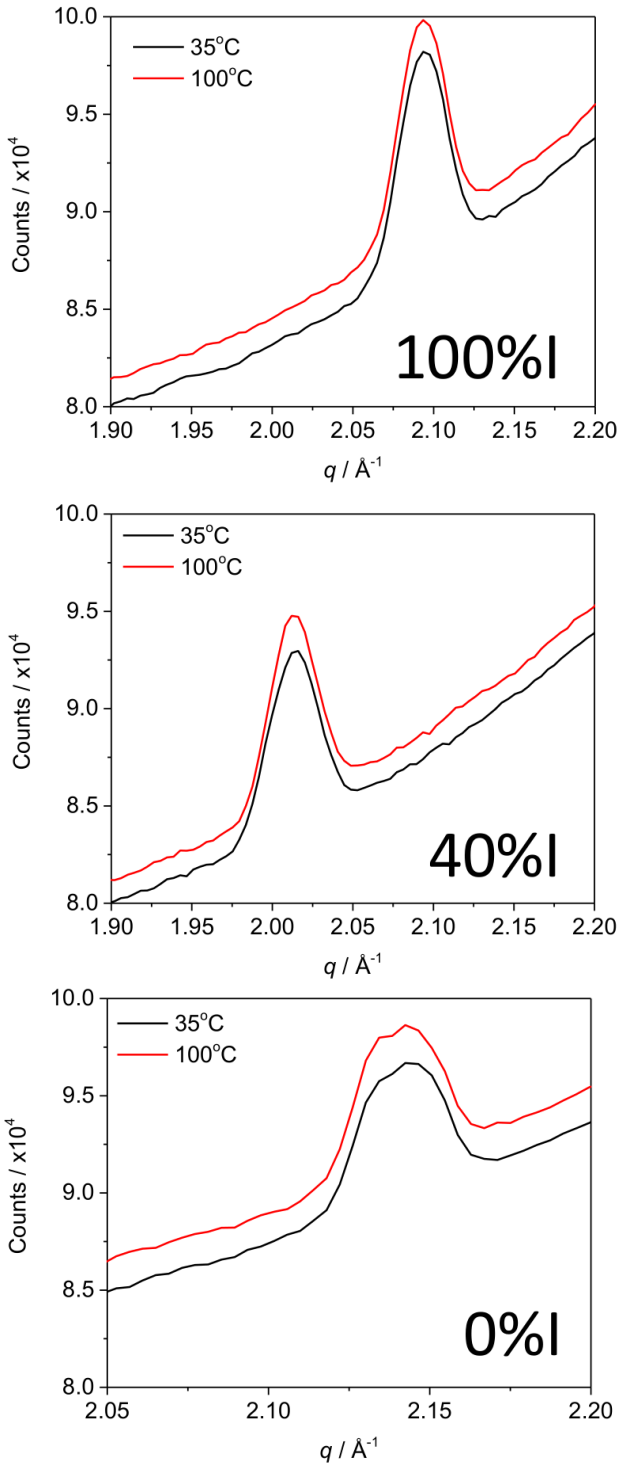


Figure S14: To confirm that the observed changes in the $MAPb(I_{1-x}Br_x)_3$ samples are not a result of local heating, WAXS was conducted on samples 35˚C and 100˚C. The resulting changes in the (220) reflection are minor, with the overall WAXS pattern dominated by thermal expansion of the substrate. The shape of the heated reflections do not exhibit the spectral shifts seen in the illuminated spectra (Figure S6) and no difference in behaviour was observed between tri-iodide, tri-bromide, and mixed-halide samples.

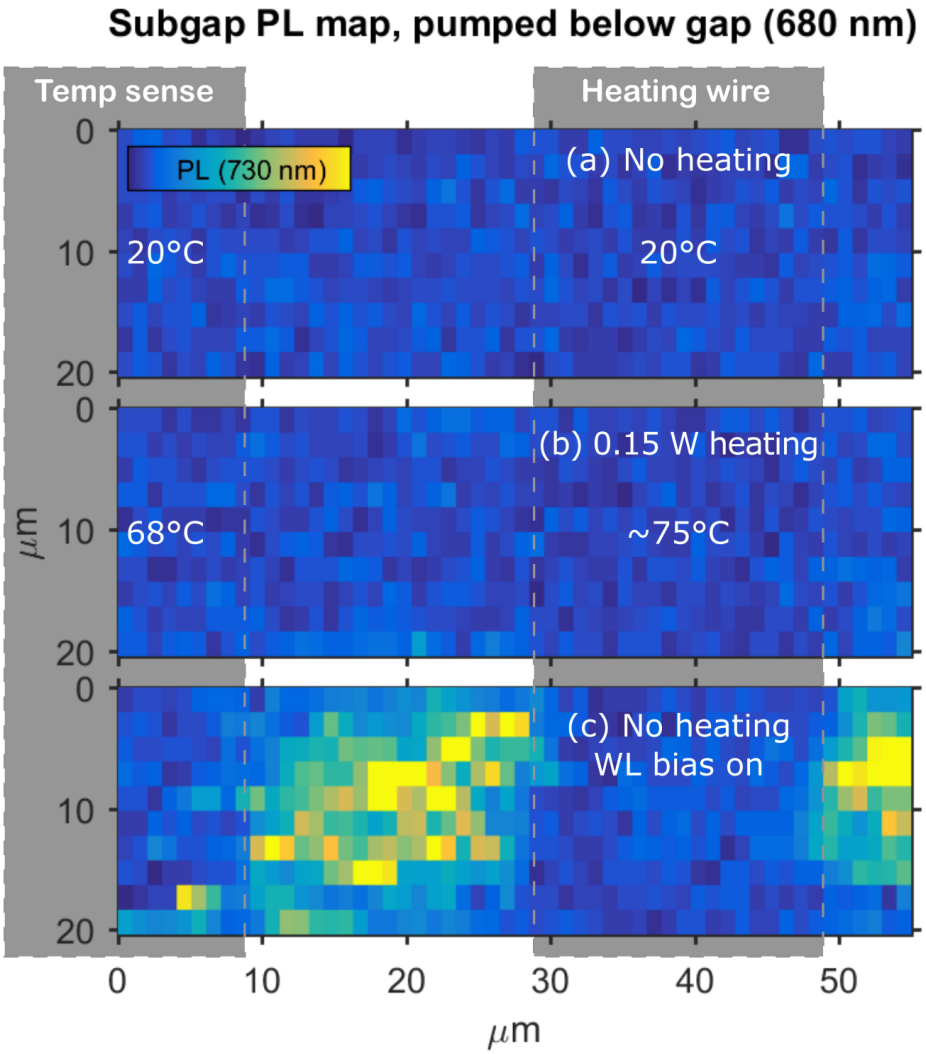


Figure S15: Confocal microscopy of subgap PL, showing that subgap formation cannot be induced by application of heat, or of a heat gradient (up to 75 degC, and 3.5×10^5 K/m, respectively).

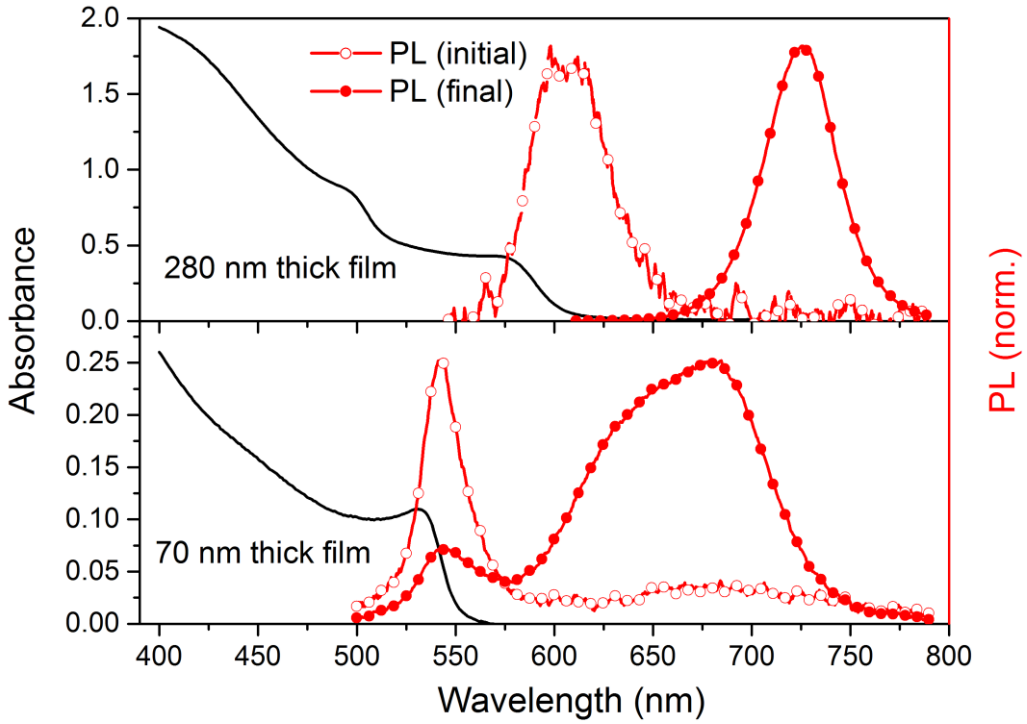


Figure S16: UV-vis absorption (black) and photoluminescence (red) for thick and thin films of $MAPb(I_{1-x}Br_x)_3$. The films show approximately equivalent absorption per unit thickness, enabling the comparison of sub-gap PL growth shown in Figure 5 of the main text as a function of film thickness. The initial and final PL spectra correspond to the initial and final times shown in Figure 5 of the main text. While the films were prepared with the same ratio of bromide and iodide precursors, differences in crystallization kinetics resulted in a difference in band gap between the two films. This makes the stability of the thin film even more impressive, since the photoinduced sub-gap PL has been shown to emerge more rapidly in films with higher bromide content[4]. PL was measured in air with excitation from a CW laser (405 nm, 0.1 W/cm^2). Film thickness was measured using a profilometer.

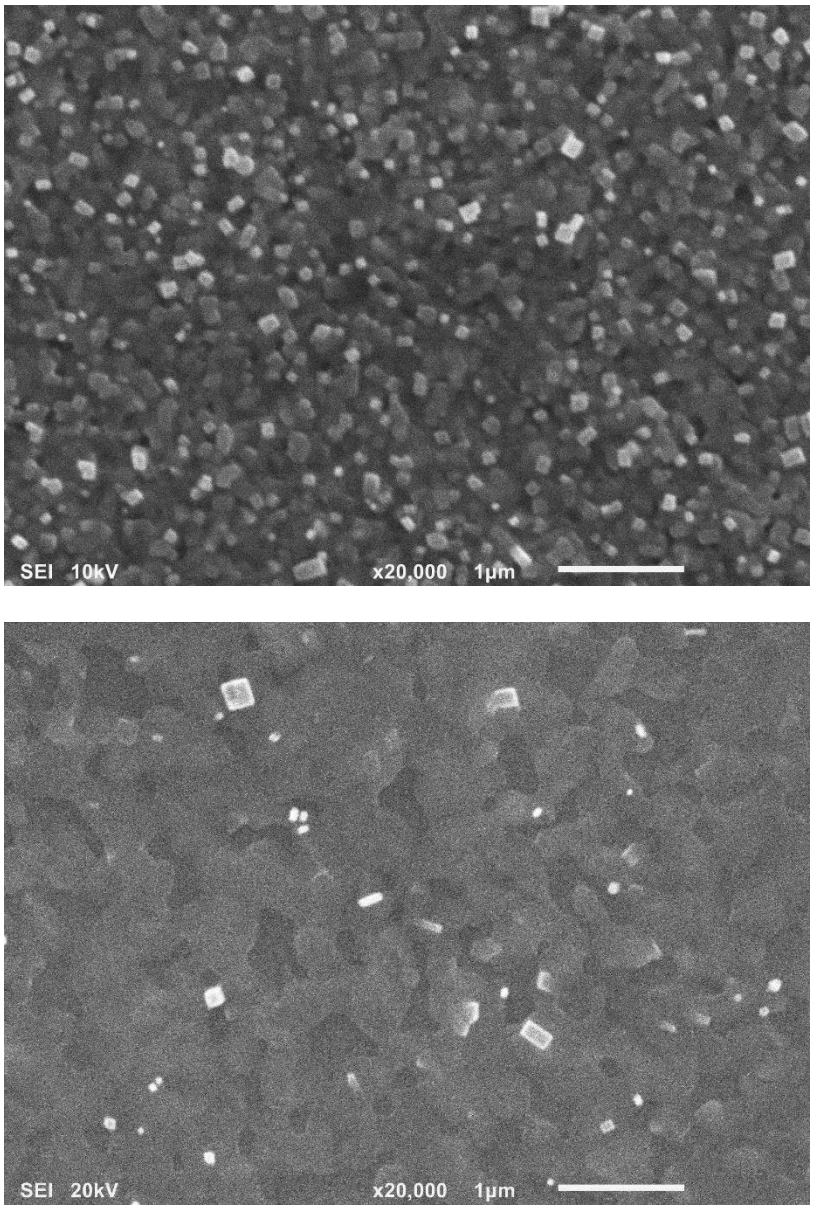


Figure S17: SEM images of the 280 nm (top) and 70 nm (bottom) thick $MAPb(I_{1-x}Br_x)_3$ films. Both films exhibit full coverage of the substrate with similar morphology, though the 70 nm film features larger and less dense capping crystals.

Supplementary Methods 1: Computational Details

Density Functional Theory (DFT) calculations have been carried out, within a planewave/pseudopotential approach, as implemented in the Quantum Espresso software package.[5] The PBE[6] exchange-correlation functional is used along with ultrasoft, scalar relativistic pseudopotentials for all atoms. Plane waves cutoffs of 25 and 200 Ry are adopted, for expansion of the wave function and density, respectively, sampling the first Brillouin zone at the Γ point only. Electron−ion interactions were described by ultrasoft pseudopotentials with electrons from O, N, and C 2s2p, H 1s, Pb 6s6p5d, I 5s5p, Br 4s4p electrons explicitly included in the calculations. Damped dynamics was used for geometry optimizations with force threshold of 1.0×10^{-4} atomic units. On the optimized geometries electronic structure calculations were performed to obtain the projected densities of states (PDOS) using both a scalar relativistic and SOC approach, respectively, see Figure S18. The $MAPbI_3$ perovskite slab was a tetragonal 2x2x4 PbI_2-temrminated slab while $MAPbBr_3$ is a cubic 3x3x4 MABr-terminated slab, see Figure S18. By combining the tetragonal iodide perovskite with the cubic bromide one, we obtained a perfect lattice matching (with a mismatching ~ 0.04%). The experimental $MAPbI_3$ cell parameters[4] (a = b = 17.71 Å) were employed to build a periodic supercell in the x and y directions, leaving 10 Å vacuum along the z direction. Car-Parrinello molecular dynamics[7] have been performed with a time step of 10 au, for a total simulation time of ca. 15 ps. The fictitious mass used for the electronic degrees of freedom is 1000 au, and we set the atomic masses to an identical the value of 5 amu to enhance the dynamical sampling. Initial ions position randomization has been used to reach the temperature in the range of 350-400 K, without further applying any thermostat.

The electronic properties of the $MAPbBr_3/MAPbI_3$ interface are summarized in the local DOS analysis shown in Figure S18. At the scalar-relativistic level of theory, our results are expected to fortuitously reproduce the band-gap of $MAPbI_3$ and to partly catch the band-gap increase observed from $MAPbI_3$ to $MAPbBr_3$.[8,9] The calculated interface electronic structure qualitatively shows the expected $MAPbBr_3/MAPbI_3$ alignment of energy levels,[4] with $MAPbBr_3$ valence (conduction) band lying below (above) the $MAPbI_3$ band edges both by scalar-relativistic and spin-orbit coupling DFT.

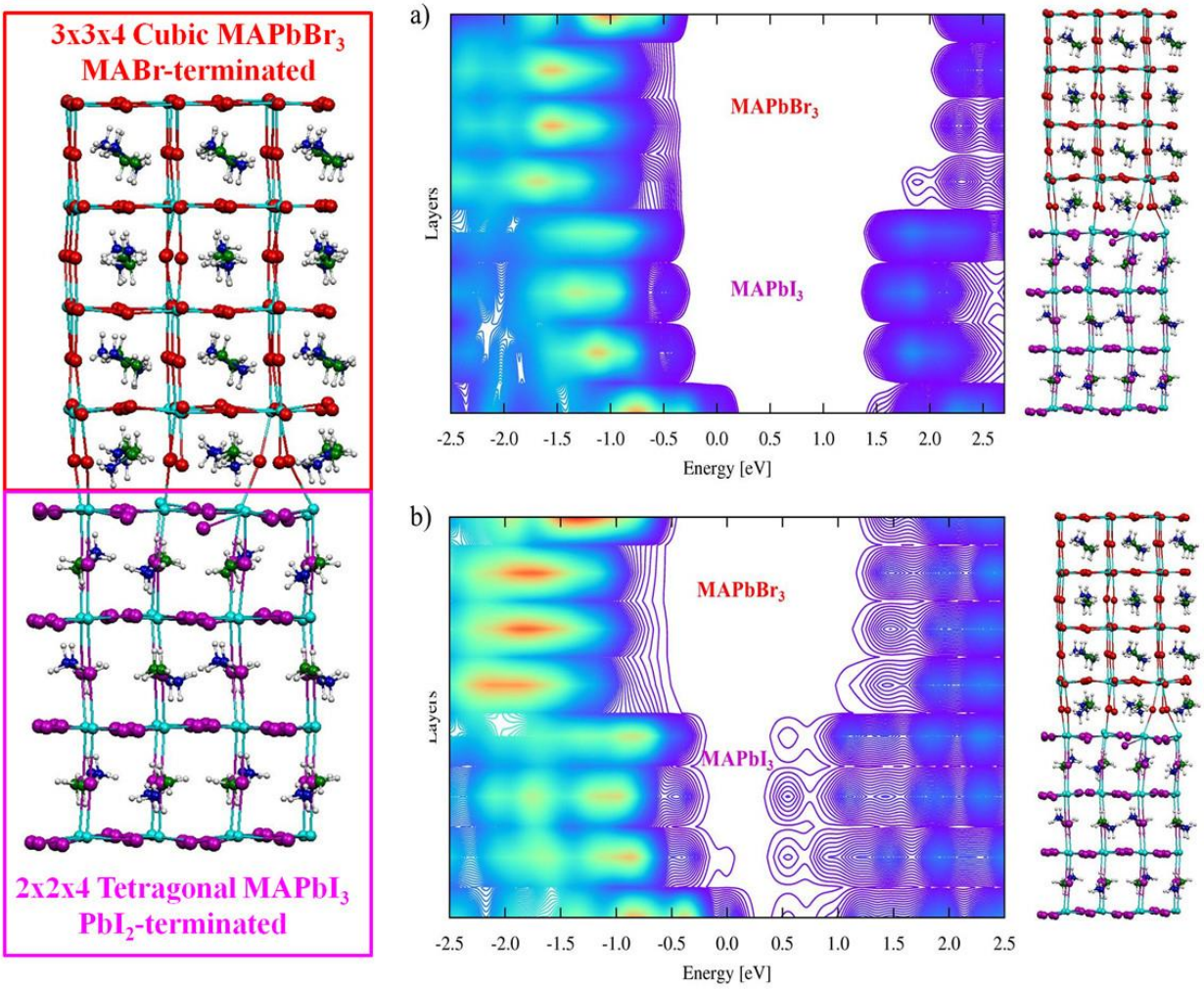


Figure S18: Calculated interface electronic structure of $MAPbBr_3/MAPbI_3$ at both (a) scalar-relativistic and (b) spin-orbit coupling DFT level of theory.

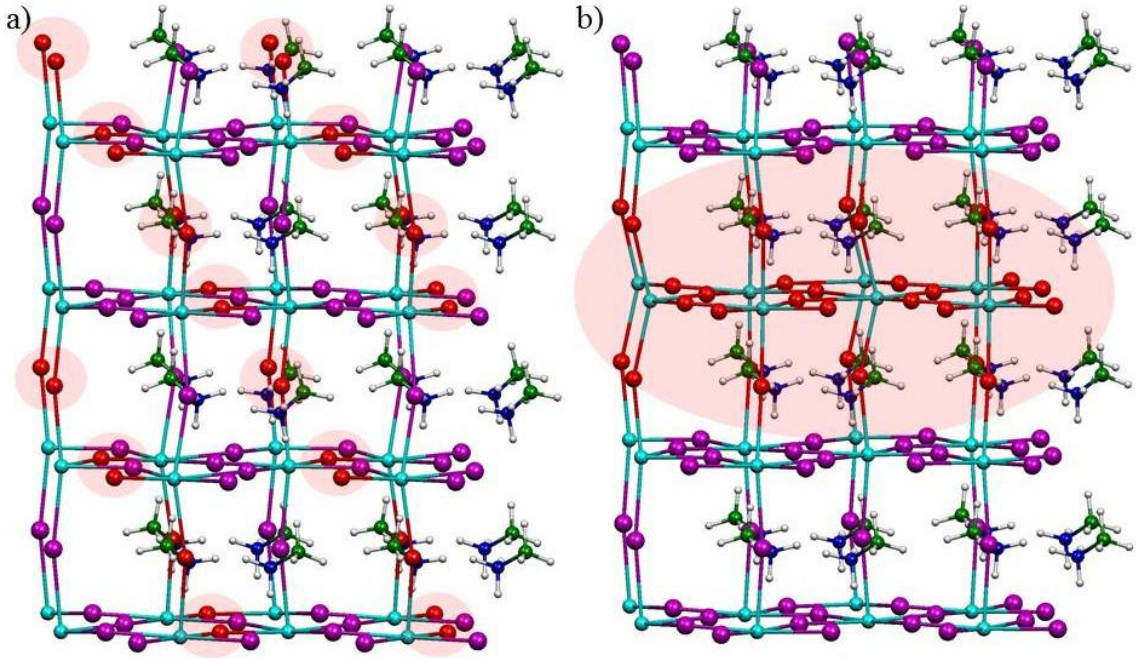


Figure S19: Bulk systems with the same 3:1 I:Br stoichiometry: (a) bromide evenly dispersed or (b) concentrated in a specific region. Iodide atoms are reported in purple and Bromide atoms in red. Red circles highlights the Br atoms.

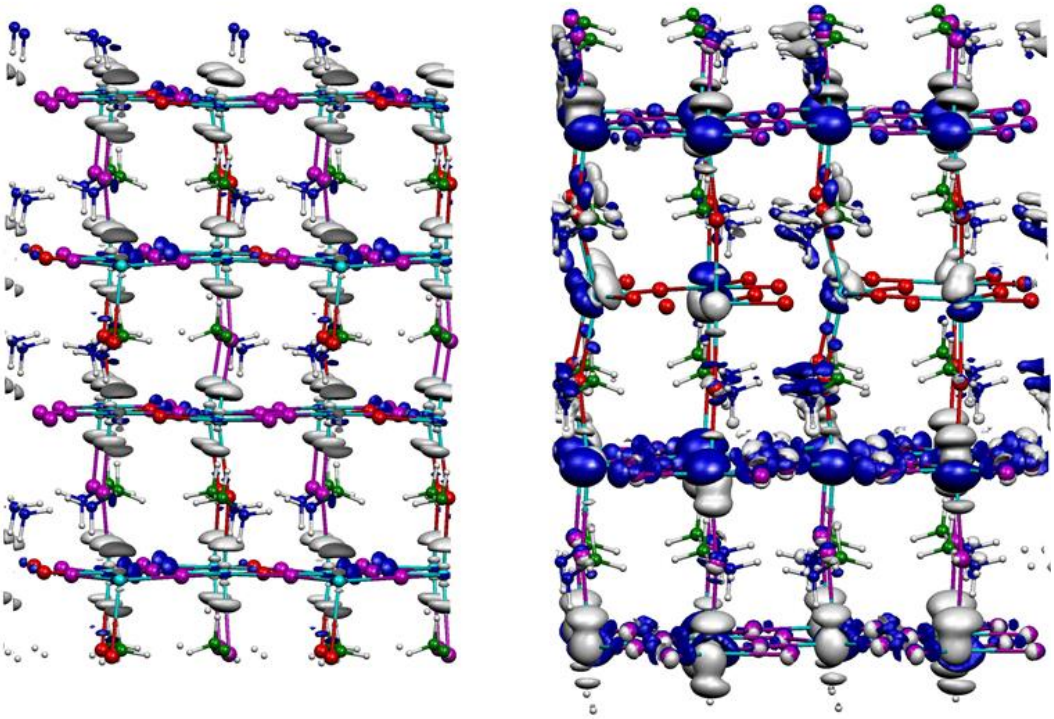


Figure S20: Charge density difference between the singlet an triplet states of the dispersed (left) and concentrated (right) systems of Figure S19. Notice the evenly distributed charge density difference for the dispersed system, opposite to the I-rich based density difference for the concentrated system (right) indicative of preferential hole localization in the I-rich domain.

Table S3. Calculated valence band maximum (VBM) and conduction band minimum (CBM) for the bromide evenly dispersed (energy set to 0) and concentrated bulk systems. The relative stabilities (eV) of the Singlet (energy set to 0) and Triplet species are also reported.

	Br Dispersed	Br Concentrated
VBM	0.00	0.07
CBM	1.86	1.86
Singlet	0.00	0.13
Triplet	1.84	1.91 (ΔE = 0.06)

References:

(1) Le Bail, A.; Duroy, H.; Fourquet, J. L. Ab-initio structure determination of LiSbWO6 by X-ray powder diffraction. *Mater. Res. Bull.* **1988**, *23*, 447–452.

(2) Rodriguez-Carvajal, J.; Fernandez-Diaz, M. T.; Martinez, J. L. Neutron diffraction study on structural and magnetic properties of La 2 NiO 4. *J. Phys. Condens. Matter* **1991**, *3*, 3215–3234.

(3) Basham, M.; Filik, J.; Wharmby, M. T.; Chang, P. C. Y.; El Kassaby, B.; Gerring, M.; Aishima, J.; Levik, K.; Pulford, B. C. A.; Sikharulidze, I.; *et al.* Data Analysis WorkbeNch (DAWN). *J. Synchrotron Radiat.* **2015**, *22*, 853–858.

(4) Poglitsch, A.; Weber, D. Dynamic disorder in methylammoniumtrihalogenoplumbates (II) observed by millimeter-wave spectroscopy. *J. Chem. Phys.* **1987**, *87*, 6373.

(5) Giannozzi, P.; Baroni, S.; Bonini, N.; Calandra, M.; Car, R.; Cavazzoni, C.; Ceresoli, D.; Chiarotti, G. L.; Cococcioni, M.; Dabo, I.; *et al.* QUANTUM ESPRESSO: a modular and open-source software project for quantum simulations of materials. *J. Phys. Condens. Matter* **2009**, *21*, 395502.

(6) Perdew, J. P.; Burke, K.; Ernzerhof, M. Generalized Gradient Approximation Made Simple. *Phys. Rev. Lett.* **1996**, *77*, 3865–3868.

(7) Car, R.; Parrinello, M. Unified Approach for Molecular Dynamics and Density-Functional Theory. *Phys. Rev. Lett.* **1985**, *55*, 2471–2474.

(8) Umari, P.; Mosconi, E.; De Angelis, F. Relativistic GW calculations on CH3NH3PbI3 and CH3NH3SnI3 perovskites for solar cell applications. *Sci. Rep.* **2014**, *4*, 4467.

(9) Even, J.; Pedesseau, L.; Jancu, J.; Katan, C. Importance of Spin–Orbit Coupling in Hybrid Organic/Inorganic Perovskites for Photovoltaic Applications. *J. Phys. Chem. Lett.* **2013**, *4*, 2999–3005.